

# Structure-dependent fragmentation risk of rubble-pile asteroids on low-impacts

Chenyang Huang,<sup>1,2</sup> Yang Yu,<sup>1,\*</sup> Peter R. King,<sup>2</sup> Bin Cheng,<sup>3</sup> and Raphael Blumenfeld<sup>4,†</sup>

<sup>1</sup>*School of Aeronautic Science and Engineering, Beihang University, Beijing 100191, China*

<sup>2</sup>*Department of Earth Science and Engineering, Imperial College London, London SW7 2BP, UK*

<sup>3</sup>*School of Aerospace Engineering, Tsinghua University, Beijing 100084, China*

<sup>4</sup>*Gonville & Caius College, University of Cambridge, Cambridge CB2 1TA, UK*

(Dated: February 27, 2024)

A key strategy in defending against stray asteroids is deflection from a collision trajectory by a low-momentum impact. This is to avoid a potential rain of large hazardous fragments, which high-momentum blasts may generate. Using a proof-of-principle numerical model, we show that even low-momentum impacts on rubble pile asteroids (RPAs), which most asteroids are, may lead to their fracturing into large fragments because of their internal non-uniform chain-like stress distribution. Since stress chains occur in three- and two-dimensional (2D) loose aggregates, we study low-momentum impacts on gravity-aggregated clusters in 2D. We establish that stresses are indeed supported by chains and show that the post-impact dynamic shear stress and displacement rates are highest along the chains, increasing significantly the risk of fracturing there. Our simulations suggest that this phenomenon is independent of the cluster's particle size distribution. We conclude that future studies must be carried out to quantify the relations between the risk of fracturing and stress chain statistics in RPAs.

Asteroid impact defense is significant for the survival of Mankind and has attracted much study. One defense strategy is to deflect an asteroid hurling toward Earth by 'shooting' at it a projectile that deflects it to a safe trajectory [1]. This strategy is often preferable to simply blasting such objects, which requires much more energy. A significant consideration in employing this strategy is to avoid too much damage to the asteroid so as not to cause its fracturing into several fragments that are sufficiently large to pass the atmosphere and reach Earth, causing even larger damage than the original asteroid. Therefore, a key issue is an estimate of the effect of the projectile's impact angle and its momentum transfer to the approaching asteroid.

Impacting relatively dense asteroids generates cratering accompanied by shattering of the impact region [2, 3]. Some of the kinetic energy of such events then 'propagates' as a shock wave of diminishing magnitude into the asteroid [4, 5] and it is important to estimate whether or not this energy can fragment the asteroid. A grazing impact is then the much safer option. However, a large fraction of asteroids are rubble-pile asteroids (RPAs), consisting of loosely connected aggregates of particles and boulders. These fragment more easily than solid asteroids and require a more careful estimate of the extent of damage under any impact parameters. The bulk densities of RPAs are low owing to high porosity [6, 7]. Moreover, loosely packed particulate aggregates are known to transmit stresses non-uniformly in the form of sparse force chain networks [8, 9], whose characteristics depend on the aggregate's internal structure. The less dense the aggregate the more non-uniform the stress field [10] and the more fragile the asteroid.

Discrete element method (DEM) studies of impact-induced seismic waves in RPAs proved a useful method to gain an understanding of such phenomena [5, 11]. However, previous studies did not consider the effects of the non-uniform and sparse force chain networks. In particular, one expects the material density to be higher along force chains than around them and, therefore, the stress response to impacts should propagate faster along such chains. Since elevated shear stress increases the risk of fracturing such a risk must be assessed. Here we test this idea and show that stress chains are indeed vulnerable. Therefore, we argue that the risk of fracturing must be taken into consideration when planning low-momentum impacts aimed only to deflect RPAs from hazardous trajectories.

Since stress in granular media is transmitted by force chains in two and three dimensions, it is sufficient and simplest to provide a proof of concept in two dimensions (2D). Therefore, we study a 2D toy model, whose main purpose is to investigate numerically and illustrate the effects of stress chains in RPAs. We find that such chains modify the response to even low-momentum impacts and significantly increase the risk of fracturing along them.

We employed the following methodology. We first constructed 2D models of rubble-pile clusters (RPCs) by aggregating under gravity particles of several size and shape distributions. We then quantified their internal structures and non-uniform stress fields, verifying that they consist of stress chains. Next, we simulated impacts at, and away from, stress points, and studied the relations between the initial stress field and the propagation characteristics of the dynamic responses of the displacement and stress fields.

For our numerical simulations, we used the in-house soft-sphere discrete-element code DEMBody [12–14]. The interparticle contact forces were nonlinear, based on the Hertz–Mindlin–Deresiewicz model [15] and deter-

\* Second corresponding author: yuyang.thu@gmail.com

† First corresponding author: rbb11@cam.ac.uk

TABLE I. Particle characteristic and contact parameters in our simulations.

Parameter	Symbol	Value
Young modulus	$Y$	$5 \times 10^9$ Pa
Poisson's ratio	$\nu$	0.3
Static friction coefficient	$\mu_s$	1.0
Dynamic friction coefficient	$\mu_d$	1.0
Restitution coefficient	$\varepsilon$	0.4
Shape parameter	$\beta$	0.8
Material density	$\rho$	$3.4 \times 10^3$ kg/m <sup>3</sup>

mined by particle overlaps, which are typically less than 1% of their size. In general, these interactions include normal and tangential components, rolling and twisting torques, and cohesion [12]. Aiming to provide only a proof of principle, our systems were confined to the plane  $z = 0$ , which obviated interparticle twisting torques. We also neglected any cohesive forces. The particle parameters, given in Table I, were chosen to mimic the mechanical properties of real 3D regolith particles and boulders on RPAs. The shape parameter,  $\beta$ , is a statistical measure that models particle non-sphericity and controls the rotational resistance to relative motions in the rolling direction [16].

An initial static 2D rubble-pile cluster (RPC) was constructed as follows. A nuclear four-particle aggregate was placed at the origin, surrounded by a cloud of  $N \approx 3000$  particles, confined to an annulus around it (Fig. 2 in the supplemental material (SM) [17]). The cloud particles are attracted to the nucleus, as well as to one another, by the gravitational forces between any two particles. The cloud particles were allowed to aggregate as they 'fell' toward the nucleus and their motion was damped to dissipate the kinetic energy on the approach to a static state. The RPC was considered static when the ratio of the total kinetic energy (translational + rotational) to the total initial gravitational potential energy of the particle cloud falls below  $10^{-6}$ . The density and porosity of the final RPC can be controlled by the initial density of the particle cloud in the annulus and the particle size distribution (PSD). We checked that the generated RPCs were mechanically stable by ascertaining that their bulk mean coordination numbers, excluding rattlers, were slightly larger than 3 [18].

Most of our investigations were carried out using an equal-numbers bi-disperse PSD:  $d_1 = 5$  m and  $d_2 = 10$  m, but we corroborated our conclusions by comparing to further simulations with a power-law PSD,  $P(d) \sim d^{-3}$ , often observed in RPAs [19–21].

Determining the stress field in an initial RPC is tricky because the particles retain small residual translational and rotational velocities, as well as residual contact torques, also known as rolling torques, generated by local elastic deformations. These lead to slightly off-symmetric stress tensors. The particle stress fields were determined, using the definition in [22, 23] and modifying it to the

particle scale,

$$\sigma_{\alpha\beta,p} = \frac{1}{A_p} \sum_{p' \in p} f_{p'p,\alpha} r_{p'p,\beta} + \frac{J_p}{A_p} (\dot{\omega}_p \varepsilon_{\alpha\beta 3} + \omega_p^2 \delta_{\alpha\beta}) . \quad (1)$$

Here,  $p'$  are the particles in contact with particle  $p$ ,  $f_{p'p,\alpha}$  the  $\alpha$ -component of the force that  $p'$  exerts on  $p$ ,  $r_{p'p,\beta}$  the  $\beta$ -component of the position vector to the contact between  $p'$  and  $p$  (see Fig. 1 in the SM [17]),  $J_p$  the moment of inertia of  $p$ ,  $\omega_p$  the angular velocity of  $p$ ,  $J_p \dot{\omega}_p$  the total torque moment applied to  $p$ ,  $\varepsilon_{\alpha\beta 3}$  the component of the Levi-Civita tensor,  $\delta_{\alpha\beta}$  the Kronecker delta, and  $A_p$  the area associated with particle  $p$ . The full stress tensor is given in the SM [17]. We determine  $A_p$  by quantifying the local disordered structure, using the quadron method [18, 24], detailed in the SM [17]. Using the quantitative characterizations of the local structure and particle stress, we visualized the traces of particle stress tensor to identify stress chains. The negative stress trace here reflects the compressive interparticle forces.

Next, we ran simulations of impacts applied to the static RPCs, designed to understand the effects of stress chains on the anisotropy and the range of damage propagation. An impact is simulated as a velocity pulse to a particle or a surface boulder. The magnitudes of the velocity pulses ranged from  $1 \times 10^{-3}$  m/s to 10 m/s, corresponding to impact momenta between  $1.78 \times 10^3$  kg·m/s and  $1.78 \times 10^7$  kg·m/s. The low limit was chosen to allow us to observe preferred directions of stress and displacement propagation, which otherwise get washed out by the extended damage caused by more violent impacts. The impact locations were chosen judiciously, to isolate effects of stress chains and impact momenta magnitudes.

To generalize our study, we use non-dimensional units of lengths, time, velocities, and stress components, respectively:

$$l_0 \equiv \bar{d} \quad ; \quad t_0 \equiv \sqrt{\frac{l_0}{\bar{g}}} \quad ; \quad v_0 \equiv \frac{l_0}{t_0} \quad ; \quad \sigma_0 \equiv \frac{\bar{m}}{t_0^2} , \quad (2)$$

such that  $t \rightarrow \tau = t/t_0$ ,  $\mathbf{v} \rightarrow \mathbf{u} = \mathbf{v}/v_0$ ,  $\sigma \rightarrow \tilde{\sigma} = \sigma/\sigma_0$ , and all lengths are in units of  $l_0$ . Here,  $\bar{d}$  is the mean particle diameter,  $\bar{g} = (G/N) \sum_i \sum_{j \neq i} m_j / |\mathbf{r}_j - \mathbf{r}_i|^2$  is the pre-impact gravitational acceleration magnitude, averaged over all the RPC particles, and  $\bar{m}$  is the mean particle mass. The size of the  $N$ -particle RPC is defined as its radius of gyration,

$$R_g = \sqrt{\frac{\sum_{i=1}^N m_i r_i^2}{\sum_{i=1}^N m_i}} . \quad (3)$$

We also define a time-dependent mean front of the propagating response:

$$D = \frac{\sum_{i=1}^N H(|\mathbf{u}_i| - |\mathbf{u}_{th}|) |\mathbf{r}_i - \mathbf{r}_{\text{impact}}|}{R_g \sum_{i=1}^N H(|\mathbf{u}_i| - |\mathbf{u}_{th}|)} , \quad (4)$$

in which  $H(x)$  is the Heaviside step function,  $|\mathbf{u}_{\text{th}}| = \alpha |\mathbf{u}_{\text{impact}}|$  is a velocity threshold,  $\mathbf{u}_i$  is the velocity of particle  $i$ , and  $\mathbf{r}_{\text{impact}}$  and  $\mathbf{r}_i$  are the position vectors of the impacted particle and particle  $i$  respectively, with the origin at the RPC's center of mass. The value of  $D$  depends somewhat on the choice of  $|\mathbf{u}_{\text{th}}|$ , but our results and conclusions are independent of it.

Three PSDs were used for the impact simulations: bi-disperse (Fig. 1), bi-disperse and larger surface boulders (Fig. 3), and power-law (Fig. 4). In all the simulations, we first verified that gravity alone generates networks of stress chains and identified the strong chains before simulating impacts.

Real impacts take place at RPAs' surfaces and we simulated such impacts. However, our main aim was to study the effect of stress chains on damage pattern and propagation. To illustrate these effects, we also mimicked impacts *inside* RPCs to take advantage of the richer choice of stress chains there. For a thorough study, impacts on particles in stress chains were applied in different directions relative to the chains. For comparison, we also applied the same impact magnitude to particles in weak-stress regions. The post-impact dynamics data were used to determine the correlations between the initial stress chains and the damage propagation pattern, speed, and range.

**Bi-disperse PSD:** We show a typical example of the gravity-induced non-uniform stress distribution in a bi-disperse system in Fig. 1(a). The probability distribution of  $|\text{Tr}(\tilde{\sigma}_0)|$  decays exponentially, as shown in Fig. 3 in the SM [17], but the probability that its magnitude is higher than 100 is only 0.0073. Impacts were then applied to large ( $M = 1.78\bar{m}$ ) 'internal' and surface particles in judiciously chosen locations. The magnitude of all the impact momenta was  $8.90 \times 10^3 \text{ kg}\cdot\text{m/s} = 1.78\bar{m}v_0$ , with  $|\mathbf{u}_{\text{impact}}| = 1$ . In Fig. 1, we show impact simulations on particle I in a stress chain in three different directions: along the chain, at  $60^\circ$  to it, and at  $90^\circ$  to it. Also shown is impacted particle II, residing in a weak-stress region at the surface. These impact simulations are labeled, respectively, as  $a - d$ .

The relations between the pre-impact stress structure and the stress and displacement rate responses are visualized in Figs. 1(b)-(d) and in Fig. 4 in the SM [17]. We present results for case  $b$ , in which the impact momentum is at  $60^\circ$  to the chain orientation, but the results are typical across all our simulations. In Fig. 1(b), we show the particles carrying strong pre-impact stress chains ( $|\text{Tr}(\tilde{\sigma}_0)| \gtrsim 20$ ) and, to study the local response, we divide the region around the impacted particle I into eight sectors. In Fig. 1(c), we show the local particle displacement rate at  $\tau = 6.63 \times 10^{-4}$  after the impact, superimposed on the pre-impact stress chains. Focusing on high stress chains, Fig. 1(d) shows the bi-variate probability of the normalized values of  $\epsilon \equiv |\text{Tr}(\tilde{\sigma}_0)| - |\text{Tr}(\tilde{\sigma}_0)|_{\text{med}}$  and  $\zeta \equiv |\tilde{\sigma}_{12}| - |\tilde{\sigma}_{12}|_{\text{med}}$ , with  $(\cdot)_{\text{med}}$  denoting the median value.

This figure, as well as more evidence in the SM [17], illustrates several points. Firstly, the displacement rate is more pronounced along the chain than in the original impact momentum direction. Secondly, the stress propagates faster along the chain than in the impact direction. Thirdly, the post-impact dynamic shear stress is also highest along the initial stress chains. In 2D, fracture could occur only under mode I and II [25]. Since we have only compressive stresses, fracture can be mainly generated by mode II, which corresponds to local shear. It is the practically causal relation between shear stress and risk of fracture that makes this observation significant. Further plots in the SM [17] (Fig. 4) and the supplemental videos, support these conclusions.

In Fig. 2, we show the dynamic response front,  $D$ , in the different sectors and its dependence on the angle between the impact momentum and the chain direction. Particle I is on a stress chain that extends into sector 5, then curves into sector 4, and continues into sector 3. Figure 2(a) confirms that  $D$  indeed propagates fastest into sector 5. At  $\tau \approx 5 \times 10^{-4}$ ,  $D$  increases dramatically in sector 4, which corresponds to the moment that the stress response carried by the chain entered sector 4. In contrast,  $D$  remains low in sectors 1, 6, 7, and 8 until this time, owing to initial low stress there or the locations opposite the impact direction. Later,  $D$  increases in sector 6 and then in 7, reflecting the eventual arrival of the stress response to these sectors along the chain path rather than directly through the medium. Figure 2(b) further corroborates the conclusion that the stress response depends on the angle between the impact and initial chain directions. It is, strongest when they are aligned (case  $a$ ) and weakest when they are perpendicular to one another (case  $c$ ).

Interestingly, the jumps in Fig. 2(a) make it possible to deduce the response propagation speed along the initial chains and potentially relate this speed to the initial stress, but this calculation is tangential to this study.

Consistent with the above, we see in Fig. 2(b) that the initial ( $\tau \lesssim 2 \times 10^{-3}$ ) response to an impact in the weak-stress region and also on a surface particle (case  $d$ ) propagates much more slowly than in case  $a$  and somewhat slower than in case  $b$ . Its speed is comparable to that in case  $c$ , in which the impact direction is also into a weak-stress region. The values of  $D$  satisfy  $a > b > c \approx d$  at all times. Past the maxima,  $D$  in case  $d$  is slightly lower than in  $c$ . In Fig. 5 in the SM [17], we show the displacement rate,  $|\mathbf{u}|$ , for the four cases at  $\tau = 6.63 \times 10^{-3}$ , superposed on the initial stress chains. A comparison of the dynamics following impacts  $a - d$  is available in the supplemental video.

**Bi-disperse PSD with surface boulders:** The bi-disperse RPCs are useful for understanding the effects of stress chains, but the real impacts take place at the surface. The near-surface of a bi-disperse aggregate is bound to support only weak stress, while surfaces of real RPAs are scattered with large boulders. Such a boulder can give rise to gravity-generated stress chains,

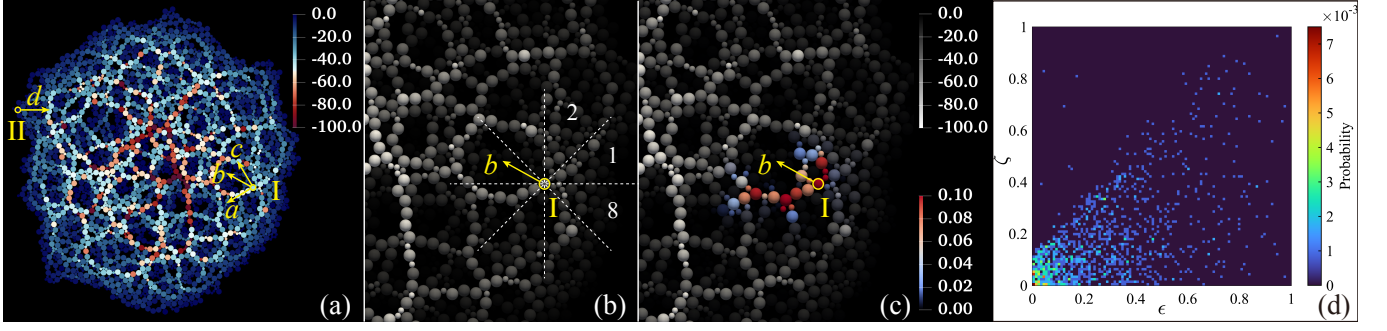


FIG. 1. An example of the bi-disperse packing and the impact tests. (a) A color map of the pre-impact  $\text{Tr}(\tilde{\sigma}_0)$ . Several impacts, labeled  $a - d$  (yellow arrows), are applied at I and II (yellow circles). (b) A zoom on  $\text{Tr}(\tilde{\sigma}_0)$  around location I, with the region around I divided into 8 sectors. (c) The particle displacement rate (blue-red) at  $\tau = 6.63 \times 10^{-4}$ , superposed on  $\text{Tr}(\tilde{\sigma}_0)$  in grey. Particles with  $|\mathbf{u}| \lesssim 0.01$  are invisible. (d) The bi-variate probability scatter map in the  $\epsilon - \zeta$  plane at  $\tau = 6.63 \times 10^{-4}$ .

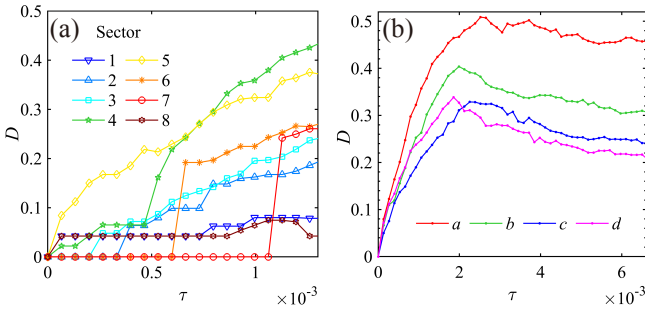


FIG. 2. The dynamic response. (a) The evolution of  $D$  in the eight sectors around I in impact test  $b$ , with  $|\mathbf{u}_{\text{th}}| = 0.01$ . (b) The evolution of the total value of  $D$  in impact tests  $a - d$ .

whose strengths depend on the boulder's and RPA's masses [14]. To assess the risk posed by these chains, we added artificially three surface boulders to our bi-disperse RPCs, of diameters  $d = 20, 40, 50$  m. After the bi-disperse RPC reached mechanical equilibrium, the boulders were released with zero velocity from a distance comparable to the RPC's  $R_g$ . Strong stress chains formed only under the two larger boulders, as can be observed in Fig. 6(a) in the SM [17]. We ran several simulations of impacts applied to the 40 m and 50 m boulders. In the following, we show the (typical) results of an impact applied to the 40 m boulder ( $M = 85.57\bar{m}$ ). The impact's momentum was  $2.26 \times 10^4$  kg·m/s  $\approx 4\bar{m}v_0$ , with  $|\mathbf{u}_{\text{impact}}| = 0.047$ , and it was directed toward the RPC's center of mass. In Fig. 3, we show the particle displacement rate (blue-red) at  $\tau = 1.71 \times 10^{-3}$  after impact, superposed on the initial stress chains (grey-scale). We verified that, in all these simulations, the displacement rate is highest along the strong stress chains, bypassing the weak-stress regions (e.g., Fig. 3(a)), and so is the shear stress response. The latter is clearly observed in Fig. 3(b) and is supported further by Fig. 6(b) in the SM [17] and the supplemental video.

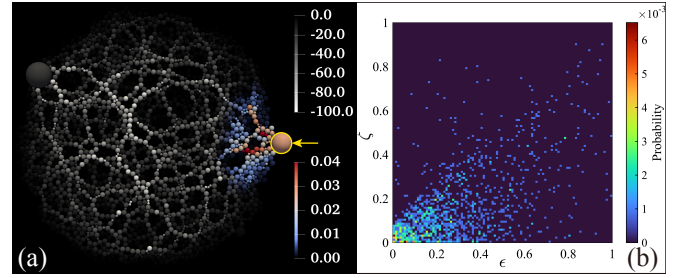


FIG. 3. (a) Particle displacement rate (blue-red) at  $\tau = 1.71 \times 10^{-3}$ , superposed on  $\text{Tr}(\tilde{\sigma}_0)$ . (b) The bi-variate probability scatter map in the  $\epsilon - \zeta$  plane at  $\tau = 1.71 \times 10^{-3}$ .

**Power-law PSD:** To ascertain that our results are not limited to bi-disperse PSDs, we ran similar simulations with a power-law PSD,  $P(d) \sim d^{-3}$ . The power was chosen, following observations in real RPAs [19–21]. The range of  $d$  was 5 – 15 m to ensure the same RPC mass as in the bi-disperse case. In Fig. 4, we show an example of the response to an impact on a particle ( $M = 1.78\bar{m}$ ) in a stress chain. The impact momentum was  $8.93 \times 10^3$  kg·m/s  $= 1.78\bar{m}v_0$  ( $|\mathbf{u}_{\text{impact}}| = 1$ ), and its direction was along the chain and perpendicular to a nearby one (see Fig. 7(a) in the SM [17]). In all simulations of these systems, we observed the same preferential response propagation in the chain direction. In Fig. 4(a), we show an example. Superposing the stress chains, particle displacement rate at  $\tau = 1.00 \times 10^{-3}$  clearly illustrates this phenomenon. In places, the high displacement rate circumvents regions of weak stress and is even perpendicular to the impact direction. Fig. 4(b) also shows that, by and large, high post-impact shear stress locations coincide with pre-impact strong stress chains. Further support is provided by the product  $\text{Tr}(\tilde{\sigma}_0) \cdot |\tilde{\sigma}_{12}|$  in Fig. 7(b) in the SM [17], which is highest along the pre-impact chains.

We ran further simulations of RPCs with the same power-law PSD and the same particle size range as the bi-disperse range, which are unavoidably less massive.



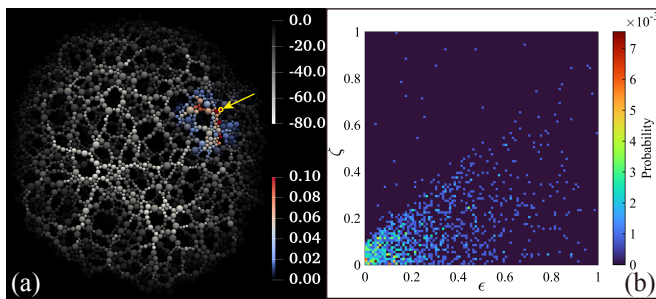


FIG. 4. Superposition of  $\text{Tr}(\bar{\sigma}_0)$  (grey-scale) and particle displacement rate (blue-red) at  $\tau = 1.00 \times 10^{-3}$ . (b) The bivariate probability scatter map of particles in the parameter space formed by  $\epsilon$  and  $\zeta$  at  $\tau = 1.00 \times 10^{-3}$ .

Those results are shown in Fig. 8 in the SM [17] and also support our conclusions that, along stress chains, the response propagates further and faster and the shear stress is generically highest.

To conclude, we set out to determine the effects of stress chains on the response of RPAs to low-momentum impacts, aimed only to change their trajectories. For proof of principle, we constructed a 2D model of random pile clusters (RPCs) and showed that pre-impact stress chains modify significantly the internal dynamic responses to impact. Specifically, the shear stress and the displacements are highest along them and they also increase the response range, depending on the relative angle between the impact direction and the orientation of the impacted stress chain. We have verified that these effects occur in both bi-disperse and power-law PSDs, suggesting that, at least in the particle size ranges we

studied, these effects are not sensitive to the PSD, although how large they might be.

Since fracturing is sensitive to the shear stress and displacements, our results show that stress chains increase significantly the risk of fragmentation along pre-existing chains even at low impact momenta and, therefore, that this risk must be assessed when attempting to merely deflect RPAs. Ways to assess this risk are downstream of this work, but they should probably include investigations into the relations between the statistical characteristics of the stress chain network (strength and spatial distributions) and the magnitudes of the dynamic shear stress and displacements. Such studies are undergoing and will be reported eventually.

## ACKNOWLEDGMENTS

C.H. is grateful for the hospitality of Imperial College London, where this work was carried out. C.H. is supported by the international joint doctoral education fund of Beihang University. Y.Y. acknowledges the financial support provided by the National Natural Science Foundation of China Grants No. 12272018.

R.B. and C.H. conceived the idea for the study; C.H., R.B., P.R.K., and Y.Y. developed the idea; C.H. conducted the simulations and the numerical analysis; B.C. is the main developer of DEMBody and assisted in resolving technical issues; C.H. and R.B. wrote the paper; P.R.K and Y.Y. reviewed and revised the paper.

- 
- [1] R. T. Daly, C. M. Ernst, O. S. Barnouin, N. L. Chabot, A. S. Rivkin, A. F. Cheng, E. Y. Adams, H. F. Agrusa, E. D. Abel, A. L. Alford, *et al.*, Successful kinetic impact into an asteroid for planetary defence, *Nature* **616**, 443 (2023).
  - [2] D. P. O'Brien, R. Greenberg, and J. E. Richardson, Craters on asteroids: Reconciling diverse impact records with a common impacting population, *Icarus* **183**, 79 (2006).
  - [3] J. Leliwa-Kopystyński, M. J. Burchell, and D. Lowen, Impact cratering and break up of the small bodies of the solar system, *Icarus* **195**, 817 (2008).
  - [4] L. R. Gómez, A. M. Turner, M. van Hecke, and V. Vitelli, Shocks near jamming, *Physical review letters* **108**, 058001 (2012).
  - [5] P. Sánchez, D. J. Scheeres, and A. C. Quillen, Transmission of a seismic wave generated by impacts on granular asteroids, *The Planetary Science Journal* **3**, 245 (2022).
  - [6] M. Grott, J. Biele, P. Michel, S. Sugita, S. Schröder, N. Sakatani, W. Neumann, S. Kameda, T. Michikami, and C. Honda, Macroporosity and grain density of rubble pile asteroid (162173) ryugu, *Journal of Geophysical Research: Planets* **125**, e2020JE006519 (2020).
  - [7] J. Biele, K. N. Burke, M. Grott, A. J. Ryan, D. DellaGiustina, B. Rozitis, P. Michel, S. Schröder, and W. Neumann, Macroporosity and grain density of rubble pile asteroid (101955) bennu, in *Proceedings of the American Geophysical Union Fall Meeting 2020* (2020).
  - [8] A. H. Clark, A. J. Petersen, L. Kondic, and R. P. Behringer, Nonlinear force propagation during granular impact, *Physical review letters* **114**, 144502 (2015).
  - [9] E. Azéma, P. Sánchez, and D. J. Scheeres, Scaling behavior of cohesive self-gravitating aggregates, *Physical Review E* **98**, 030901 (2018).
  - [10] M. Cates, J. Wittmer, J.-P. Bouchaud, and P. Claudin, Jamming, force chains, and fragile matter, *Physica Review Letters* **81**, 1841 (1998).
  - [11] G. Tancredi, P.-Y. Liu, A. Campo-Bagatin, F. Moreno, and B. Domínguez, Lofting of low-speed ejecta produced in the dart experiment and production of a dust cloud, *Monthly Notices of the Royal Astronomical Society* **522**, 2403 (2023).
  - [12] B. Cheng, Y. Yu, and H. Baoyin, Collision-based understanding of the force law in granular impact dynamics, *Physical Review E* **98**, 012901 (2018).
  - [13] B. Cheng, Y. Yu, and H. Baoyin, Numerical simulations

- of the controlled motion of a hopping asteroid lander on the regolith surface, *Monthly Notices of the Royal Astronomical Society* **485**, 3088 (2019).
- [14] B. Cheng, Y. Yu, E. Asphaug, P. Michel, D. C. Richardson, M. Hirabayashi, M. Yoshikawa, and H. Baoyin, Reconstructing the formation history of top-shaped asteroids from the surface boulder distribution, *Nature Astronomy* **5**, 134 (2021).
  - [15] E. Somfai, J.-N. Roux, J. H. Snoeijer, M. Van Hecke, and W. Van Saarloos, Elastic wave propagation in confined granular systems, *Physical Review E* **72**, 021301 (2005).
  - [16] M. Jiang, Z. Shen, and J. Wang, A novel three-dimensional contact model for granulates incorporating rolling and twisting resistances, *Computers and Geotechnics* **65**, 147 (2015).
  - [17] Supplemental material, containing details of the stress calculation, additional figures, and two videos.
  - [18] R. C. Ball and R. Blumenfeld, Stress field in granular systems: loop forces and potential formulation, *Physical review letters* **88**, 115505 (2002).
  - [19] D. DellaGiustina, J. Emery, D. Golish, B. Rozitis, C. Bennett, K. Burke, R.-L. Ballouz, K. Becker, P. Christensen, C. Drouet d'Aubigny, *et al.*, Properties of rubble-pile asteroid (101955) bennu from osiris-rex imaging and thermal analysis, *Nature Astronomy* **3**, 341 (2019).
  - [20] S. Mazrouei, M. Daly, O. S. Barnouin, C. Ernst, and I. DeSouza, Block distributions on itokawa, *Icarus* **229**, 181 (2014).
  - [21] T. Michikami, C. Honda, H. Miyamoto, M. Hirabayashi, A. Hagermann, T. Irie, K. Nomura, C. M. Ernst, M. Kawamura, K. Sugimoto, *et al.*, Boulder size and shape distributions on asteroid ryugu, *Icarus* **331**, 179 (2019).
  - [22] F. Nicot, N. Hadda, M. Guessasma, J. Fortin, and O. Millet, On the definition of the stress tensor in granular media, *International Journal of Solids and Structures* **50**, 2508 (2013).
  - [23] B. Yan and R. A. Regueiro, Definition and symmetry of averaged stress tensor in granular media and its 3d dem inspection under static and dynamic conditions, *International Journal of Solids and Structures* **161**, 243 (2019).
  - [24] R. Blumenfeld, Stresses in isostatic granular systems and emergence of force chains, *Physical review letters* **93**, 108301 (2004).
  - [25] L. B. Freund, *Dynamic fracture mechanics* (Cambridge university press, 1998).